International Journal of Heat and Mass Transfer 180 (2021) 121757

Contents lists available at ScienceDirect

International Journal of Heat and Mass Transfer

journal homepage: www.elsevier.com/locate/hmt

Charging optimization of multi-tube latent heat storage comprising composite aluminum foam/nano-enhanced coconut oil

Seyed Mohsen Hashem Zadeh[a], Maryam Ghodrat[b], Kaamran Raahemifar[c,d,e], Obai Younis[f,g], Mohammad Ghalambaz[h,i,*]

[a] School of Engineering and Information Technology, University of New South Wales Canberra, Canberra 2610 ACT, Australia
[b] School of Engineering and Information Technology, University of New South Wales Canberra, Canberra 2610 ACT, Australia
[c] College of Information Sciences and Technology (IST), Data Science and Artificial Intelligence Program, Penn State University, State College, Pennsylvania, PA 16801, United States
[d] School of Optometry and Vision Science, Faculty of Science, Dept. of Chemical Engineering, Faculty of Engineering, University of Waterloo 200 University Ave W, Waterloo, ON N2L 3G1, Canada
[e] Electrical and Computer Engineering Dept., Sultan Qaboos University, Muscat, Sultanate of Oman
[f] Department of Mechanical Engineering, College of Engineering at Wadi Addwaser, Prince Sattam Bin Abdulaziz University, Saudi Arabia
[g] Department of Mechanical Engineering, Faculty of Engineering, University of Khartoum, Sudan
[h] Metamaterials for Mechanical, Biomechanical and Multiphysical Applications Research Group, Ton Duc Thang University, Ho Chi Minh City, Vietnam
[i] Faculty of Applied Sciences, Ton Duc Thang University, Ho Chi Minh City, Vietnam

ARTICLE INFO

Article history:
Received 8 February 2021
Revised 27 June 2021
Accepted 18 July 2021
Available online 2 August 2021

Keywords:
Latent heat thermal energy storage
Fast charging
Metal foam
Optimum design

ABSTRACT

The fast charging of thermal energy storage (TES) systems is a requirement for the practical application of these systems. The thermal energy should be stored in a unit within a reasonable time. The present research aims to minimize the thermal charging time of a latent heat TES unit by using aluminium foams, nanoparticles (copper oxide), and geometrical optimization of the unit. The melting phase change was simulated in the TES unit by using FEM. The Taguchi optimization method was invoked to maximize the melting rate during two hours of thermal charging. The results showed that the geometrical design of the unit and the porosity of foam are the most influential design parameters on the thermal energy storage and melting rate. The variation of the design parameters could improve the melting rate by 41%. The presence of nanoparticles could only improve the melting rate by less than 2%. The optimal design of the TES unit can be fully charged in two hours. Such fast-charging time could be advantageous in solar systems and transient heat recovery.

1. Introduction

Many thermal systems deal with transient heating/cooling loads. Thus, devices with the capability to store/release thermal energy could essentially damp possible mismatches between production and demand. For example, solar systems could produce heat during day time, but consumption of heat could occur during evening or night times. The thermal energy storage could store/release a notable amount of energy on demand. The latent heat TES units can store a considerable amount of thermal energy in the form of latent heat of phase change in a compact space [1]. The latent heat TES systems use the phase change material (PCM) for the porpoise of energy storage. Organic PCMs, such as paraffin wax, can store a considerable amount of latent heat energy [2]. Thus, organic materials are excellent candidates for TES units in many domestic and industrial applications. However, the thermal conductivity of organic material is low. For example, paraffin wax's thermal conductivity is just 0.21 W/(m K) [3], which is even several times lower than water. The low thermal conductivity of PCMs results in a slow heat transfer process and a long response time (charging/discharging time). Thus, special attention to TES units' design is required to improve their thermal response.

Some researchers tried to improve the heat transfer of TES units by using fins. For example, Shahsavar et al. [4] applied swirl fins to improve heat transfer and reduce the melting time. The TES unit with swirl fins reduced the charging time of the unit by 54%. Shinde et al. [5] employed radial fins on the heat transfer tubes to improve the thermal energy release rate. A portion for a fin was

* Corresponding author.
E-mail addresses: s.hashem_zadeh@adfa.edu.au (S.M. Hashem Zadeh), m.ghodrat@unsw.edu.au (M. Ghodrat), Kraahemi@gmail.com (K. Raahemifar), oubeytaha@hotmail.com (O. Younis), mohammad.ghalambaz@tdtu.edu.vn (M. Ghalambaz).

https://doi.org/10.1016/j.ijheatmasstransfer.2021.121757
0017-9310/

Latin symbols

A_{mushy}	Constant of the mushy zone
ES	Amount of energy stored in the storage
C_p	Specific heat capacity
d_p	Pore size
d_l	Ligament diameter
g	Acceleration of gravity
L_{sf}	Latent heat of the PCM
k	Thermal conductivity coefficient
K	Permeability of the porous media
MVF	Melted volume fraction
p	Pressure field
P	Charging power
r_{im}	Inner radius of pipe no. m
r_{om}	Outer radius of pipe no. m
S/N	Signal to Noise (ratio)
t	Pipe thickness, time
T	Temperature
ΔT	Phase change temperature range
T_{melt}	Melting temperature
u	velocity component in x-direction
v	velocity component in y-direction

Greek symbols

μ	Dynamic viscosity
β	Coefficient of thermal expansion
ε	Porosity of the porous media
ξ	Pore density
σ	Melt volume fraction in the elements
ρ	Density
ω	Volume fraction of nanoparticles

Subscripts

in	Initial value
CuO	CuO nanoparticle
mf	Metal foam
eff	Effective value
s	Solid
i	Phase indicator (i.e., liquid or solid)
k	Domain indicator (i.e., NePCM#1 or NePCM#2)
sw	Solid wall
PCM	Phase change material
$nPCM$	Nano-enhanced Phase change material
l	Liquid

in the heat transfer tube and another portion in the PCM domain. Thus, the fins directly absorb the PCM heat inside the TES unit and transfer it to the fluid inside the heat transfer tube. The results showed that there is an optimum design for the fin design. Tiari et al. [6] utilized a network of copper tubes as fins (heat pipes) and investigated the charging and discharging time of a cylindrical TES unit. The tubes' temperature could be controlled by the circulation of heat transfer fluid (HTF). The results showed that the charging time of the TES unit is under the significant influence of flow circulations while the heat transfer in tubes had minimal impact on the discharging process. A 300% increase in HTF flow circulation reduced the discharging time by only 6.5%. Generally, using fins could locally boost the thermal conductivity and direct heat into a PCM domain, but the thermal diffusion and melting/solidification process rely on the thermal conductivity of the PCM, which is quite low.

An interesting approach to improve the heat transfer rate of PCMs is the dynamic melting enhancement technique. A pump can circulate the melted PCM in the LHTES enclosure in the dynamic melting technique. Gasia et al. [7] investigated the dynamic melting of a shell and tube Latent Heat Thermal Energy Storage (LHTES) module with a small circulation follow of melted PCM. The results showed that the melting period was reduced by 30.9% when the liquid PCM circulation velocity was only 0.025 m/s. Tay et al. [8] examined the dynamic melting in a tube-in-tank PCM storage system and observed that the system could be effective for HTF with high flow rates. Xiong et al. [9] and Yang [10] investigated the dynamic melting of PCMs in a U-tube heat exchanger and a helical coil heat exchanger, respectively. Both of these studies also showed heat transfer enhancement by using dynamic melting. Partial loading is is another approach for the improvement of the charging/discharging time. The concept comes from the fact that an LHTES module with a low fraction of melting liquid can better absorb the heat and be charged compared to a module with high fraction of liquid (high charged percentages). Thus, depending on the load demands and time of energy avability, the charging fraction of a module can be adjusted for maximum heat transfer rate [11–13].

Some researchers utilized open metal foams to improve the thermal conductivity of PCM uniformly. The PCM was embedded in the foam structure, and thus, the foam acts as a thermal-conductive structure and contributes to heat transfer and melting/solidification of the PCM inside the pores. Zhu et al. [14] investigated the impact of using copper foam on the melting heat transfer of a heatsink. A portion of the heatsink was filled with copper foam, and the rest was pure PCM. The results showed that the presence of the copper foam could enhance the melting rate notably. El Idi et al. [15] synthesized paraffin/metal foam composite PCMs using a vacuum method. The thermal conductivity of paraffin/metal foam was improved by 18 folds compared to the pure Paraffin. Duan and Li [16] experimentally examined the effect of pore density and porosity of a copper foam on the melting heat transfer. The results showed that the porosity has a major impact on the charging time (melting rate) while the pore size has a minimal effect on charging time.

The addition of thermal conductive nanoparticles to the PCM and the synthesizing of nano-enhanced Phase Change Materials (NePCM) is another approach to uniformly improve the thermal conductivity of a PCM [17,18]. Selvaraj et al. [19] synthesized samples of NePCMs and measured the samples' dynamic viscosity and thermal conductivity. They compared the measurement data with the well-known Brinkman and Maxwell models. The results showed ±4% uncertainty for evaluating dynamic viscosity using the Brinkman model, while the Maxwell model could evaluate the thermal conductivity by ±2% uncertainty. Faraji et al. [20] examined the thermal behaviour of NePCMs in a heatsink enclosure. The n-eicosane was adopted as PCM, and the impact of four nanoparticle types, Al_2O_3, ZnO, CuO, and Cu, on the melting phase change was analyzed. The results showed that using nanoparticles improves heat transfer and decreases the temperature of electronic components. The hybrid use of nanoparticles could further improve heat transfer. Akash et al. [21] examined the melting process of NePCMs in a concentric cylindrical enclosure. These researchers showed that using alumina nanoparticles can enhance the melting rate. Other researchers such as [22,23] also used nano-additives to improve the heat transfer in TES systems.

Some researchers have used the integration of foams and nanoparticles to add improvement to the heat transfer rate. Mahdi et al. [24] used a combination of NePCMs and metal foam in a triplex-tube latent heat energy storage system. They reach up to a 90% reduction in the charging time of the TES unit. They find that a dense metal foam (low porosity) and high concentration of nanoparticles could further reduce the charging time. However, they recommended a porous medium with high porosity and only a low volume fraction of nanoparticles.

Table 1
Thermophysical properties of the coconut oil, nano-additives of copper oxide, aluminium foam, and copper [25–28].

Properties	Coconut oil				
	Liquid	Solid	CuO	Aluminium	Cu
Specific heat (J/kg/K)	2010	3750	5400	765	386
Density (kg/m^3)	914	920	6500	3970	8920
Thermal conductivity (W/m/K)	0.166	0.228	18	40	401
Thermal expansion coefficient (1/K)	1.167×10^{-3}	–	8.5×10^{-6}	–	–
Fusion temperature (°C)	24	–	–	–	–
Kinematic viscosity (Ns/m^2)	0.0326	–	–	–	–
Latent heat (kJ/kg)	103	–	–	–	–

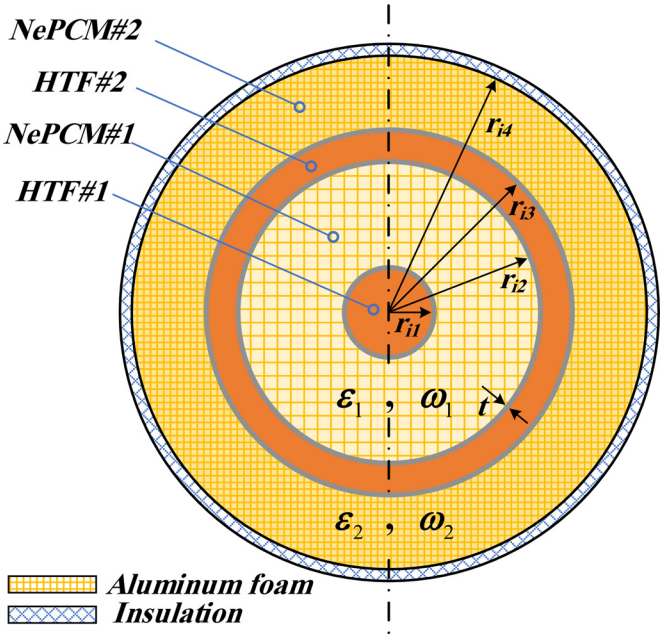

Fig. 1. Schematic view of the multi-tube latent heat energy storage unit (the figure is not to scale).

The present study aims to analyze a cylindrical TES unit using a combination of metal foam, nanoparticles, and geometrical improvement of the enclosure for the first time. The Taguchi method is employed to maximize the melting rate by optimizing the design parameters.

2. Mathematical model

The 2D schematic view of the LHTES unit is outlined in Fig 1. As shown, the storage is divided into four distinct regions using three impermeable circular tubes. The gold regions denote the location of NePCMs (NePCM#1 and NePCM#2), the orange ones show the heat transfer fluid area (HTF#1 and HTF#2), and the gray ones are the solid walls of the tubes. Coconut oil is the energy storage medium, and the tubes are made from copper. Moreover, to improve the charging performance of the LHTES, PCMs are first enhanced with copper oxide nanoparticles (CuO) and then embedded in the aluminum foam. Thermophysical properties of the employed PCM, nano-additives, HTF, metal foam and the solid walls are presented in Table 1. To charge the storage, water is used as the heat transfer fluid and pumped through the designed spaces for the HTF. The shell of the storage is well insulated and considered adiabatic. Initially, the storage is kept isothermally at T_{in} = 288 K, and the HTFs will start to flow through the tubes. The storage is designed so that HTF#1 flows through the inner pipe with an inner radius of r_{i1} and then enters the annulus area of HTF#2 in a counter-current direction. As such, to have an equal flow rate in both HTFs, the surface area of the inner domain and annulus region associated with HTF#2 are the same. Since the temperature difference between the inlet and outlet of HTF is low [4], the charging process of the storage can be simplified and simulated in a 2D computational domain (Fig. 1-b). This means that the temperature on the inner surfaces of the HTF#1 and HTF#2 pipes can be considered isothermally as T_h. The inner radii of the tubes are shown as r_{im} (m = 1:4) in Fig. 1. The thickness of all tubes is the same and equals t = 1 mm. The outer radii of the tube can be obtained as $r_{om} = r_{im} + t$ (m = 1:3). Owing to the symmetry of the model, only half of the domain is numerically analyzed.

The governing equations for the storage, including the nano-enhanced phase change substance, metal foam, and the solid walls, are [29–31]:

Conservation of mass:

$$\left(\frac{\partial u}{\partial x}+\frac{\partial v}{\partial y}\right)=0, \tag{1}$$

Conservation of momentum in x- and y- directions:

$$\frac{\rho_{nPCM-k}}{\varepsilon_k^2}\left(\varepsilon_k\frac{\partial u}{\partial t}+u\frac{\partial u}{\partial x}+v\frac{\partial u}{\partial y}\right) = -\frac{\partial p}{\partial x}+\frac{\mu_{nPCM-k}}{\varepsilon_k}\left(\frac{\partial^2 u}{\partial x^2}+\frac{\partial^2 u}{\partial y^2}\right)+Bu, \tag{2}$$

$$\frac{\rho_{nPCM-k}}{\varepsilon_k^2}\left(\varepsilon_k\frac{\partial v}{\partial t}+u\frac{\partial v}{\partial x}+v\frac{\partial v}{\partial y}\right) = -\frac{\partial p}{\partial y}+\frac{\mu_{nPCM-k}}{\varepsilon_k}\left(\frac{\partial^2 v}{\partial x^2}+\frac{\partial^2 v}{\partial y^2}\right) +Bv+\rho_{nPCM-k}g\beta_{nPCM-k}(T-T_{melt}), \tag{3}$$

Conservation of energy for NePCMs:

$$(\rho C_p)_{nPCM-k}\left(\frac{\partial T}{\partial t}+u\frac{\partial T}{\partial x}+v\frac{\partial T}{\partial y}\right)=k_{eff-k}\left(\frac{\partial^2 T}{\partial x^2}+\frac{\partial^2 T}{\partial y^2}\right) -\rho_{nPCM-k}L_{sf,nPCM-k}\frac{\partial \sigma}{\partial t}, \tag{4}$$

Conservation of energy for the solid copper walls:

$$(\rho C_p)_{sw}\frac{\partial T}{\partial t}=k_{sw}\left(\frac{\partial^2 T}{\partial x^2}+\frac{\partial^2 T}{\partial y^2}\right), \tag{5}$$

In the above equations, subscripts *sw* and *nPCM* denote the solid wall and Nano-enhanced PCM, respectively. The coefficient B in Eqs. (2) and (3) is the sum of Darcy term and porosity function, respectively, and reads as:

$$B=\frac{\mu_{nPCM-k}}{K_k}-A_{mushy}\frac{(1-\sigma)^2}{\sigma^3+\varsigma}, \tag{6}$$

where K is the permeability of metal foam, and ς=0.001 is a small number and is added to avoid approaching zero in the denominator of Eq. 6 during computations. A_{mushy}, constant of the mushy zone, is, in fact, a damping factor to model the fluid flow in the mushy zone as fluid flow in a porous medium [32,33]. σ is the melting fraction of the NePCM and can be calculated as:

$$\sigma = \begin{cases} 0 & T < T_{melt} - \Delta T/2 \\ \frac{T-T_{melt}}{\Delta T} + \frac{1}{2} & T_{melt} - \Delta T/2 < T < T_{melt} + \Delta T/2 \\ 1 & T > T_{melt} + \Delta T/2 \end{cases}, \tag{7}$$

where ΔT is the phase change temperature range, and $L_{sf,nPCM}$ in Eq. 4 is the latent heat of the NePCM. The metal foam's permeability (K) is given as [24,34,35]:

$$K_k = d_p^2 \frac{73 \times 10^{-5}}{(3\pi\,\tau_k)^{0.224}} \left(\frac{d_l}{d_p}\right)_k^{1.11}, \tag{8a}$$

in the above equation, d_l is called the ligament diameter and d_p is the pore size and both could be obtained from the below equations:

$$\left(\frac{d_l}{d_p}\right)_k = 1.18(\tau_k)^{0.5}[1 - \exp(-(3\pi\,\tau_k)/0.04)]^{-1}, \tag{8b}$$

$$d_p = 254 \times 10^{-4} \xi^{-1}(PPI), \tag{8c}$$

$$\tau_k = \frac{1-\varepsilon_k}{3\pi}, \tag{8d}$$

As discussed by Ranut [36], numerous relations have been proposed for the effective thermal conductivity of the porous matrix and metal foam. The most prominent and widely-used equation is the following [37,38]:

$$k_{eff-k} = \frac{\left[k_{nPCM,i-k} + \pi(\sqrt{\tau_k} - \tau_k)\Delta k\right]\left[k_{nPCM,i-k} + (\tau_k \pi)\Delta k\right]}{k_{nPCM,i-k} + \Delta k\left[\pi\sqrt{\tau_k} + \frac{4}{3}\sqrt{\tau_k}(1-\varepsilon_k) - (1-\varepsilon_k)\right]} \quad i = l, s, \tag{9}$$

in which Δk=$k_{mf} - k_{nPCM,i-k}$ and $\tau_k$is defined in Eq. (8d). In the above equations, the difference between the thermal conductivity of the Nano-enhanced PCM is taken into consideration and hence, the subscript $i = l, s$ refers to the phase of the NePCM. Moreover, the effective heat capacity in Eq. (4) can be evaluated based on the volume average of the NePCM and aluminum foam as:

$$(\rho C_p)_{eff-k} = (1-\varepsilon_k)(\rho C_p)_{nPCM-k} + \varepsilon_k(\rho C_p)_{mf}, \tag{10}$$

where the subscript *mf* refers to the aluminium foam.

Thermo-physical characteristics of the NePCM

The density and thermal expansion coefficient of NePCM are evaluated as [39,40]:

$$\rho_{nPCM-k}(T) = \rho_{nPCM,l-k}\sigma(T) + (1-\sigma(T))\rho_{nPCM,s-k}, \tag{11a}$$

$$\rho_{nPCM,i-k} = \rho_{PCM,i} + \omega_k(\rho_{CuO} - \rho_{PCM,i}) \quad i = l, s, \tag{11b}$$

$$\rho_{nPCM,l-k}\beta_{nPCM,l-k} = \rho_{PCM,l}\beta_{PCM,l} + \omega_k\left(\rho_{CuO}\beta_{CuO} - \rho_{PCM,l}\beta_{PCM,l}\right), \tag{12}$$

in which ω_k (k =1, 2) is the volume concentration of nanoparticles.

The experimental investigation of Selvaraj et al. [19] shows that the Maxwell model and the Brinkman model can adequately evaluate the effective thermal conductivity and dynamic viscosity of NePCMs. Hence, here the Maxwell and Brinkman models were utilized to compute the effective dynamic viscosity and thermal conductivity of the NePCM [39,41]:

$$\mu_{nPCM,l-k} = \mu_{PCM,l}(1-\omega_k)^{-2.5} \tag{13}$$

$$k_{nPCM-k} = \sigma(T)k_{nPCM,l-k} + (1-\sigma(T))k_{nPCM,s-k}, \tag{14a}$$

$$k_{nPCM,i-k} = \frac{(k_{CuO} + 2k_{PCM,i}) - 2\omega_k(k_{PCM,i} - k_{CuO})}{(k_{CuO} + 2k_{PCM,i}) + \omega_k(k_{PCM,i} - k_{CuO})}\, k_{PCM,i} \quad i = l, s, \tag{14b}$$

The Brinkman model and Maxwell model (Eq. 14(b)) were adopted for the evaluation of dynamic viscosity and thermal conductivity of the NePCM, respectively.

Ultimately, the effective heat capacity and the effective latent heat of the NePCM are obtained as:

$$(\rho C_p)_{nPCM-k} = \sigma(T)(\rho C_p)_{nPCM,l-k} + (1-\sigma(T))(\rho C_p)_{nPCM,s-k}, \tag{15a}$$

$$(\rho C_p)_{nPCM,i-k} = (\rho C_p)_{PCM,i} + \omega_k\left((\rho C_p)_{CuO} - (\rho C_p)_{PCM,i}\right) \quad i = l, s, \tag{15b}$$

$$\rho_{nPCM,l-k}L_{sf,nPCM-k} = (1-\omega_k)\rho_{PCM,l}L_{sf,PCM}, \tag{16}$$

Initial and boundary conditions

The continuity of heat flux and temperature was applied at the wall-NePCM interface:

$$T|_{sw} = T|_{nPCM},\ k_{nPCM}\left.\frac{\partial T}{\partial n}\right|_{nPCM} = k_{sw}\left.\frac{\partial T}{\partial n}\right|_{sw}, \tag{17a}$$

The no-slip and zero heat flux were also employed for the insulated shell ($\sqrt{x^2+y^2} = r_{i4}$) as:

$$\text{on shell surface: } u = 0,\ v = 0, \partial T/\partial n = 0 \tag{17b}$$

where n surfaces normal. The symmetry boundary condition is considered along the vertical symmetrical line ($x = 0, 0 \le |y - r_{o1}| \le (r_{i2} - r_{o1})$ & $0 \le |y - r_{o3}| \le (r_{i4} - r_{o3})$):

$$\frac{\partial u}{\partial x} = \frac{\partial T}{\partial x} = 0, \tag{17c}$$

Further, the surface of the solid walls that are in direct contact with the HTFs are considered isothermal ($\sqrt{x^2+y^2} = r_{i1}/r_{o2}/r_{i3}$):

$$T = T_h = 305\,\text{K}, \tag{17d}$$

The NePCM is at a uniform initial super cold temperature as:

$$T = T_{in} = 288\,\text{K}, \tag{18}$$

The storage capacity (ES) of the unit a combination of sensible and latent heat stored in PCM and sensible heat in walls, which can be computed by integration over the unit surface:

$$ES = \sum_{k=1}^{2}\left\{\int_{A_{nPCM-k}}\left[(\rho C_p)_{nPCM-k}(T - T_{in}) + \rho_{nPCM,l-k}L_{sf,nPCM-k}\right]dA\right\} + \int_{A_{sw}}(\rho C_p)_{sw}(T - T_{in})dA \tag{19}$$

Ultimately, the melt volume fraction MVF, the total amount of molten PCM, was computed by integration of local melt fraction over the NePCM domains:

$$MVF = \frac{\sum_{k=1}^{2}\left\{\int_{A_{nPCM-k}}\sigma(T)dA\right\}}{\sum_{k=1}^{2}\{A_{nPCM-k}\}}, \tag{19}$$

Table 2
Details of the studied grids.

Case study	Case I	Case II	Case III	Case IV	Case V
No. of Elements	15200	22440	35550	51660	81600
Computation time	3h 57 min	5h 26 min	8h 57 min	18h 55 min	19 h 17 min
MVF at 1500s	0.83112	0.83102	0.83101	0.83097	0.83096

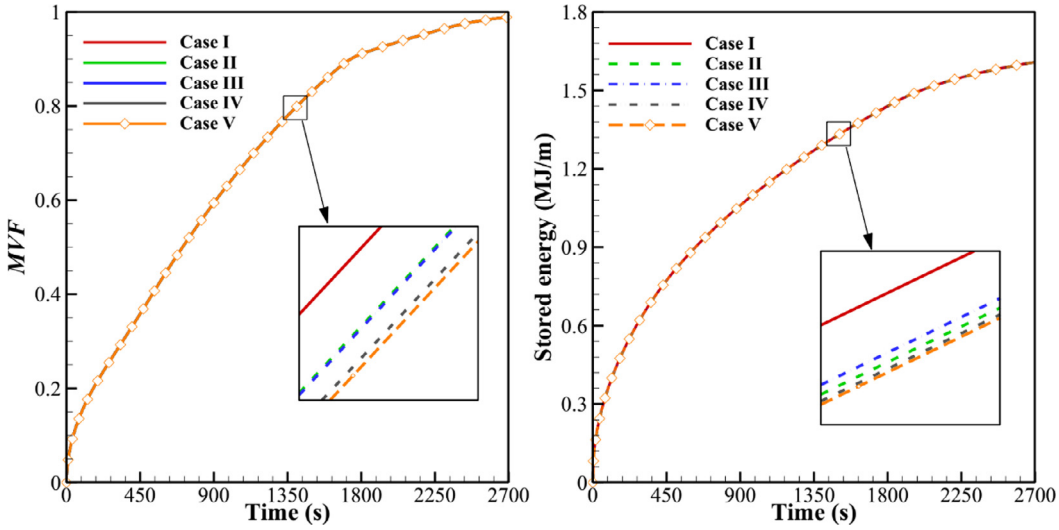

Fig. 2. *MVF* (left) and Stored energy (right) as a function of time for different mesh sizes.

3. Numerical procedure, grid test, and code validation

The partial differential equations that govern the melting process of the nano-enhanced composite coconut oil-aluminum foam Eqs. 1-(4) and the heat conduction equation in the solid walls Eq. 5) along with the discussed set of boundary and initial conditions (Eqs. 17 and (18) were solved using the commercial computational fluid dynamics package, COMSOL Multiphysics 5.4. In COMSOL Multiphysics, the equations are first transformed into the so-called weak form and then expanded using a set of basis functions for each variable (in the present study, *u, v, p,* and *T*). Subsequently, by employing the Galerkin Finite Element Method, the expanded weak form of the governing equations is written as a set of residual equations and integrated by utilizing a 2nd-order technique called Gaussian-quadrature. Further, to deal with the transient behavior of the equations, preventing numerical divergence and minimizing the overall computation time, a free step Backward Differentiation Formula (BDF) is employed to manage the size of the time steps with a variable 1^{st}- or 2^{nd}- order. The set of residual equations are solved iteratively by the Newton method using the PARDISO solver (PARallel DIrect SOlver). Also, a relative tolerance of 10^{-4}, and a manual damping factor of 0.8 is considered. The mushy zone constant is an important parameter as discussed in [42–44]. Here, it was selected to be $A_{mushy} = 5\times10^5$ based on the validation of the model with experimental results of Al-Jethelah et al. [26] for coconut oil-aluminium foam composite. Finally, to address the flow field in the mushy and solid zones, user-defined functions of the temperature field were adopted for the liquid fraction (σ) and the porosity functions (B).

Five different non-uniform structured grids, with ascending resolutions (cases I-V), shown in Table 2, were studied to perceive the appropriate grid for the computations. Two factors, including the melted volume fraction (*MVF*) of the NePCM as well as the amount of stored energy were chosen for grid check. The results are plotted in Fig. 2. It is evident that throughout the melting process, an insignificant difference between the profiles of the *MVF* and local temperatures could be observed between all the cases of I-V. However, to be on the safe side, the grid with 35550 elements (case III) we selected for the computations.

To ensure that the developed numerical code is valid and reliable, a comparison has been made between the results of the present study and the experimental study of Al-Jethelah et al. [26]. In [26], a rectangular cavity (5.0×7.2 cm^2) with three adiabatic walls was analyzed. The left wall is heated continuously through an electric heater with a variable heat load. More details about the thermophysical properties of the phase change substance and the porous medium are listed in Table 3 of [26]. The results are presented in Figs. 3. The phase change problem of pure coconut oil-aluminium foam by experimentations of Al-Jethelah et al. [26] has been selected for comparison. The melting interface of the developed code well resembles the experimental data at different simulation times of 1080s, 1440s and 2160s.. Also, the average value of the liquid fraction (*MVF*) has been computed and reported as a quantitative measurement. A maximum 8% discrepancy can be found that could be attributed to the usual heat loss and uncertainties during experimentations. Hence, the present numerical model is reliable for the analysis of the current problem.

4. Taguchi design of numerical experiments

Coconut oil is used as the phase change material in both regions of the storage, and the total amount of pure PCM in the storage is constant and equal to 0.01 m^2. As such, by dispersion of nano-additives and embedding in metal foam, the outer radius of the storage expands to store the specified amount of PCM. Moreover, the inner radius r_{i1} corresponding to the HTF#1 is assumed to be fixed at $r_{i1} = 0.019$ m. The surface areas of the HTFs are equal. Further, it is assumed that the r_{o2} (or r_{i2}) is variable, and hence, the r_{o3} (or r_{i3}) can be obtained by equating the surface area of HTF#1 and HTF#2. For instance, for the optimum case (described in Table 7), the geometrical values are presented in Table 4. CuO nano-additives and aluminium foam are employed at both regions

Table 3
The range and levels of control parameters.

Factors	Description	Level 1	Level 2	Level 3	Level 4
A	ω_1 (volume fraction of particles in the first section)	0	0.015	0.03	0.045
B	ω_2 (volume fraction of particles in the second section)	0	0.015	0.03	0.045
C	ε_1 (porosity of metal foam in the first section)	0.8	0.85	0.9	0.95
D	ε_2 (porosity of metal foam in the second section)	0.80	0.85	0.9	0.95
E	r_{o2} (the radius of the narrow heating channel)	50	60	70	80

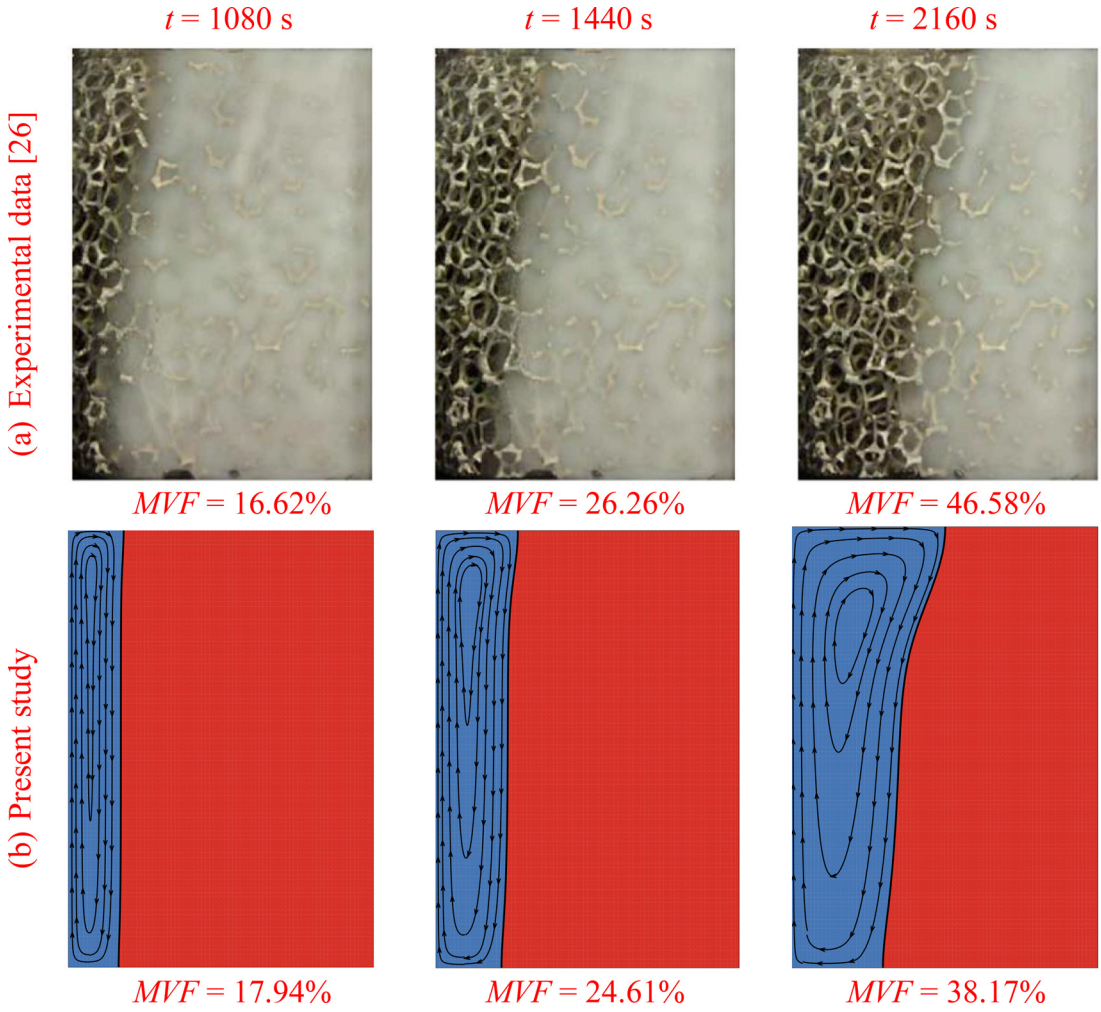

Fig. 3. Melting front during phase change of pure coconut oil in aluminum foam (0.0% CuO mass fraction): (a) experimental results of Al-Jethelah et al. [26]; (b) present study.

Table 4
Geometrical parameters of the optimum case.

r_{i1} (mm)	r_{o1} (mm)	r_{i2} (mm)	r_{o2} (mm)	r_{i3} (mm)	r_{o3} (mm)	r_{i4} (mm)
19	20	69	70	72.533	73.533	96.177

of the unit. The volume concentration of the CuO nano-additive on each side varies between 0.0 to 0.045% and is independent of the other side. In addition, the porosity of the metal foam on each side can independently vary between 0.8 to 0.95.

The major parameters of the present TES unit are the volume fractions of nanoparticles in each PCM domain (ω_1 and ω_2), the porosity of metal foam in each section (ε_1 and ε_2), and the radius of the narrow heating channel (r_{o2}). The Taguchi Method is applied to find the highest charging rate during two hours of charging time. Based on the Taguchi method, the design parameters must be divided into several levels. There are several standard orthogonal tables such as L4, L9, L12, L16, and L27, which can be used for the Taguchi method. Indeed, the orthogonal tables efficiently explore the design space with a minimum number of examinations. More details about the Taguchi method can be found in [45,46]. Here, four levels were considered for each parameter. The details of each level were brought in Table 3. Using four levels for each design variable could provide a fair splitting step for each design variable.

Since there are five design parameters and four variable the design space is consist of 4^5 possible causes. The simulation of transient phase change for such a huge design space is not practical.

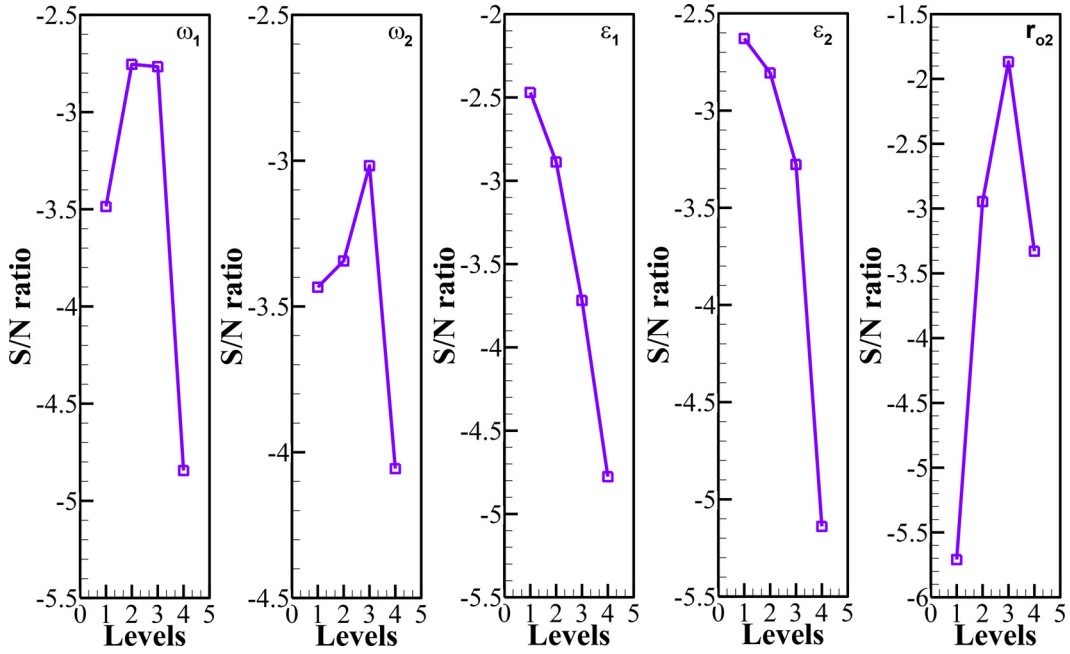

Fig 4. Signal to noise ratios based on Taguchi method: Optimum levels for A, B, C, D, and E are 3, 3, 1, 1, and 3, respectively.

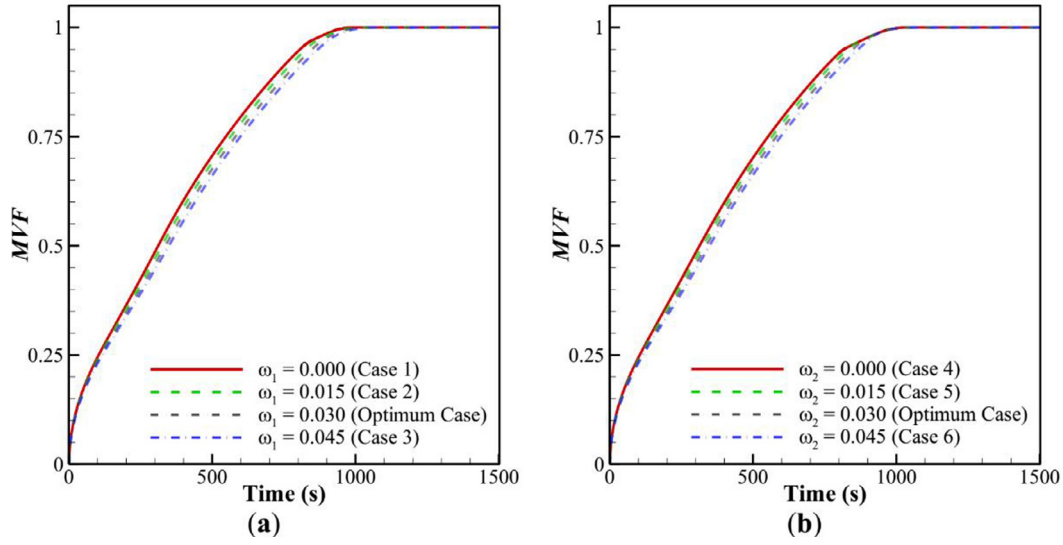

Fig. 5. Dependency of the Melting volume fraction (*MVF*) when $\varepsilon_1 = 0.8$, $\varepsilon_2 = 0.8$, and $r_{o2} = 70$ mm on the volume fraction of the CuO: (**a**) NePCM#1 (ω_1) and ω_2 =0.03 (b) NePCM#2 (ω_2) and $\omega_1 = 0.03$.

Thus, Taguchi invokes an orthogonal table to sample the design space and find an optimum design out of 4^5 possibilities. Based on the number of parameters and levels, there could be several possible standard orthogonal tables. Here, an L16 standard table was selected, which can provide an orthogonal search space with a minimum number of samples (numerical tests). As depicted in Table 5, each row of the L16 corresponds to a possible design where the simulations should be carried out. The last columns of the L16 table report the values of *MVF, ES* (kJ/m), and Power (kW/m) for each simulated case. The aim is to maximize *MVF* after two hours of charging. Here, the S/N ratio was computed based on the Taguchi method, which introduces the goodness of each design with respect to the design goal.

A design with a higher S/N ratio is better. Then, the Taguchi Method utilizes the computed S/N ratios and propose the optimum levels for design parameters. Thus, the proposed optimum case could be inside or outside the L16 (any case from 4^5 design space).

5. Results and discussion

Here, the S/N ratios are summarized in a ranking table as produced following the Taguchi method. The delta parameter indicates the variation of the S/N ratio following the variation of each parameter. The higher the variation the more influential the parameter. Rank 1 denotes a parameter with the highest influence on the *MVF*. As seen, the radius of the narrow heating channel r_{o2} is the most important design parameter. After that, the porosities are important. The volume fractions of nanoparticles are the less important parameters. The results of Table 6 are visualized in Fig. 4, so the variation of S/N ratios could be better observed. As mentioned, a level of a parameter with the highest S/N ratio is the potential level for maximum melting rate. Therefore, the optimum design

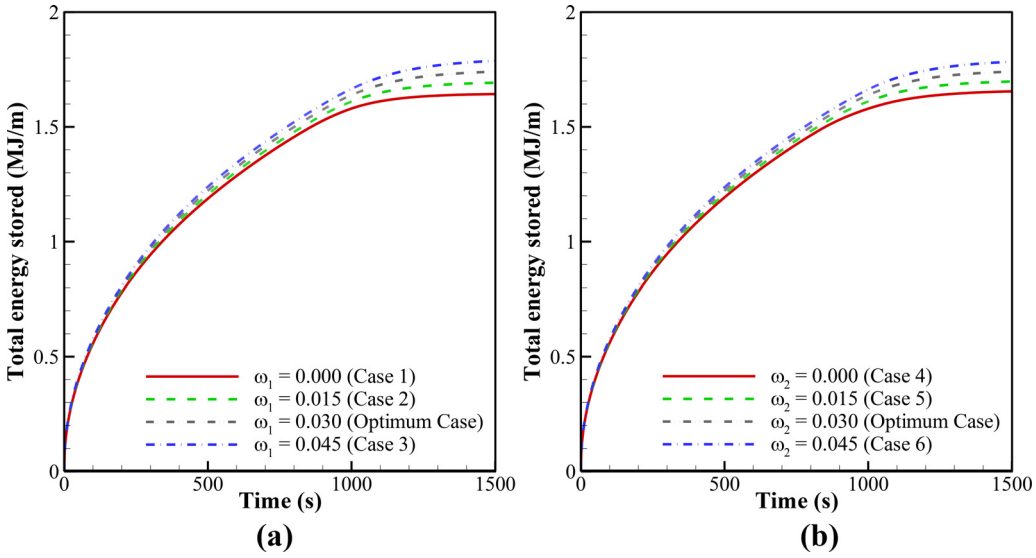

Fig. 6. Dependency of the stored energy when $\varepsilon_1 = 0.8$, $\varepsilon_2 = 0.8$, and $r_{o2} = 70$ mm on the volume fraction of the CuO: (**a**) NePCM#1 (ω_1) and ω_2 =0.03 (**b**) NePCM#2 (ω_2) and $\omega_1 = 0.03$.

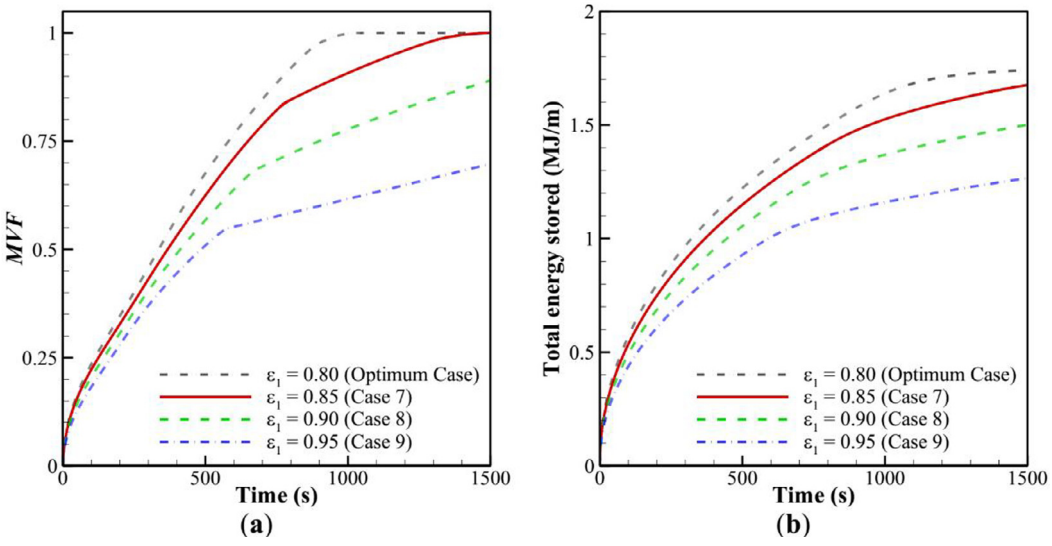

Fig. 7. Effect of porosity of aluminum foam in the inner region (ε_1) on the: (**a**) Melted fraction; (**b**) total energy stored (other parameters are same as the optimum case: $\omega_2 = 0.03$, $\omega_1 = 0.03$, $\varepsilon_2 = 0.8$, and $r_{o2} = 70$ mm).

Table 5
Taguchi L16 orthogonal table corresponding to range and levels of control parameters.

Test No.	Parameters					Data at 1200s			
	ω_1	ω_2	ε_1	ε_2	r_{o2}	*MVF*	*ES (kJ/m)*	*P= ES/Time (kW/m)*	S/N Ratio
1	0.000	0.000	0.80	0.80	50	0.64	1081	900.6	-3.876
2	0.000	0.015	0.85	0.85	60	0.83	1306	1088.6	-1.618
3	0.000	0.030	0.90	0.90	70	0.84	1299	1082.6	-1.514
4	0.000	0.045	0.95	0.95	80	0.45	826	688.1	-6.936
5	0.015	0.000	0.85	0.90	80	0.81	1288	1073.3	-1.830
6	0.015	0.015	0.80	0.95	70	0.82	1344	1120.4	-1.724
7	0.015	0.030	0.95	0.80	60	0.77	1261	1050.5	-2.270
8	0.015	0.045	0.90	0.85	50	0.55	1083	902.7	-5.193
9	0.030	0.000	0.90	0.95	60	0.62	1033	860.9	-4.152
10	0.030	0.015	0.95	0.90	50	0.50	912	760.2	-6.021
11	0.030	0.030	0.80	0.85	80	0.94	1562	1302.0	-0.537
12	0.030	0.045	0.85	0.80	70	0.96	1636	1363.0	-0.355
13	0.045	0.000	0.95	0.85	70	0.64	1153	960.8	-3.876
14	0.045	0.015	0.90	0.80	80	0.63	1201	1001.2	-4.013
15	0.045	0.030	0.85	0.95	50	0.41	842	701.5	-7.744
16	0.045	0.045	0.80	0.90	60	0.65	1287	1072.6	-3.742

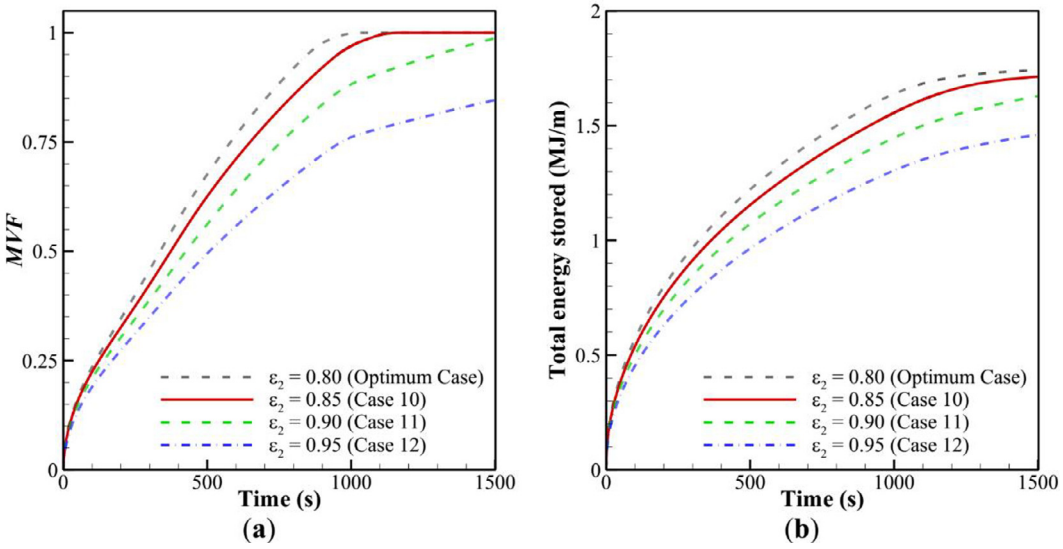

Fig. 8. Effect of porosity of aluminum foam in the outer region (ε_2) when (other parameters are same as the optimum case: $\omega_2 = 0.03$, $\omega_1 = 0.03$, $\varepsilon_1 = 0.8$, and $r_{o2} = 70$ mm) for: (**a**) Melted fraction; (**b**) total energy stored.

Table 6
The S/N and rank of design parameters based on the Taguchi method.

Levels	ω_1	ω_2	ε_1	ε_2	r_{o2}
1	-3.486	-3.434	-2.470	-2.629	-5.709
2	-2.754	-3.344	-2.887	-2.806	-2.946
3	-2.766	-3.017	-3.718	-3.277	-1.867
4	-4.844	-4.056	-4.776	-5.139	-3.329
Delta	2.090	1.040	2.306	2.510	3.841
Rank	4	5	3	2	1

Table 7
The optimum values of the design parameters.

Optimum Factors					Optimum *MVF* at 1200s	
ω_1	ω_2	ε_1	ε_2	r_{o2} (mm)	Taguchi prediction	Tested case
0.03	0.03	0.8	0.8	70	1.06	0.999

Levels for parameters of ω_1, ω_2, ε_1, ε_2, and r_{o2} are 3, 3, 1, 1, and 3, respectively. The estimated *MVF* after two hours of thermal charring is 1.06. It is clear that this number is not physically practical since the *MVF* could not adopt any value higher than unity. However, the value of 1.06 could be considered as a strong full melting for the optimum case. The design values of the optimum case are summarized in Table 7.

A simulation was carried out for this design, and the *MVF* was found as 0.999, which supports the estimated value by the Taguchi method.

Using the data of the orthogonal table L16, a linear relation for *MVF* (after two hours of charging) was computed as follow:

$$MVF|_{1200s} = -14027 + 31842\omega_1 + 6172\omega_2 + 6981\varepsilon_1 + 16188\varepsilon_2 - 63.5r_{o2}(\text{mm}), \quad (20)$$

The reported data for *MVF* in Tables 5 and 7 shows that the *MVF* can be varied from 0.59 (case13) to 0.96 (case 7) and even 1.0 for the optimum case, during two hours of charging. Thus, the design parameters can change the charging rate of TES by 41%.

The optimum case has been further analyzed around the optimum set of parameters to ensure about the performance of the TES system at the optimized configuration and also to investigate the impact of each parameter on the charging process. In this stage, the complete charging process of the storage is studied and hence, the simulation time is higher (1500s). Details of the test numbers are presented in Table 8.

Fig. 5 shows the influence of the volume fraction of nanoparticles on the *MVF*. At the beginning of charging, where the entire TES unit is in a super cold solid-state, nanoparticles' presence does not alter the melting behavior and stored energy. However, as the melting commences and natural convection circulation occurs, the impact of the nanoparticles *MVF* pronounces. As seen, the increase of nanoparticle concentrations could increase or decrease the *MVF*. This could be due to the competition between the improvement of the thermal conductivity of PCM and the increase of viscosity due to the addition of nanoparticles. The viscosity resists against the fluid motion, and an increase of viscosity reduces the benefit of natural convection. The effect of nanoparticles on the temperature and *MVF* contours was minimal, and thus, the related contours were not plotted for the sake of brevity.

Fig. 6 depicts the impact of nanoparticles of CuO on the amount of energy stored in the storage. It is worth noting that, As discussed earlier, a fixed volume of coconut oil is considered in the storage. By dispersion of the nanoparticles (or changing the porosity of the aluminium foam), the outer diameter of the storage expands. In other words, the mass of the materials in the storage is varied when the volume fraction of the nanoparticles changes. This means that the amount of energy in the form of latent heat is constant, and the difference between the shown cases is due to the sensible form of energy. According to Fig. 6, dispersion of the nanoparticles increases the amount of stored energy. This is plausible since the mass of the storage increases, and hence, a higher amount of storage can be stored in the TES system.

In addition, it can be seen that the rate of energy storage (the slope of the *ES*) is very high at the early stages of the melting process and decreases gradually as time elapses. This can be explained by the fact that, as the melting process proceeds, the average temperature difference between the HTF and the NePCMs decreases and hence, the amount of energy that could be absorbed reduces. The rate of energy storage approaches zero (constant *ES*) when the *MVF* = 1.0, indicating that the thermal equilibrium is achieved and no heat can be transferred between the HTF and the NePCMs.

Figs. 7 and 8 show the impact of porosity on the *MVF* and stored energy. These figures show that the increase of porosity significantly reduces the *MVF* and the stored energy. In the initial phase of the charging process t < 500s where the *MVF* is low,

Table 8
Further analysis around the optimum case (ω_1=0.03, ω_2=0.03, ε_1=0.8, ε_2=0.8, and r_o=70 mm).

Test No.	Parameter	Control Parameters					*MVF* at 900s	*MVF* at 1200s
		A ω_1	B ω_2	C ε_1	D ε_2	E r_{o2}		
1	ω_1	0	0.03	0.8	0.80	70	0.99	1.00
2		0.015	0.03	0.8	0.80	70	0.98	1.00
3		0.045	0.03	0.8	0.80	70	0.97	1.00
4	ω_2	0.03	0	0.8	0.80	70	0.98	1.00
5		0.03	0.015	0.8	0.80	70	0.98	1.00
6		0.03	0.045	0.8	0.80	70	0.97	1.00
7	ε_1	0.03	0.03	0.85	0.80	70	0.88	0.96
8		0.03	0.03	0.9	0.80	70	0.75	0.83
9		0.03	0.03	0.95	0.80	70	0.60	0.65
10	ε_2	0.03	0.03	0.8	0.85	70	0.92	1.00
11		0.03	0.03	0.8	0.9	70	0.84	0.93
12		0.03	0.03	0.8	0.95	70	0.72	0.80
13	r_o	0.03	0.03	0.8	0.80	50	0.51	0.59
14		0.03	0.03	0.8	0.80	60	0.75	0.84
15		0.03	0.03	0.8	0.80	80	0.83	0.94
16	Optimum	0.03	0.03	0.8	0.80	70	0.98	1.00

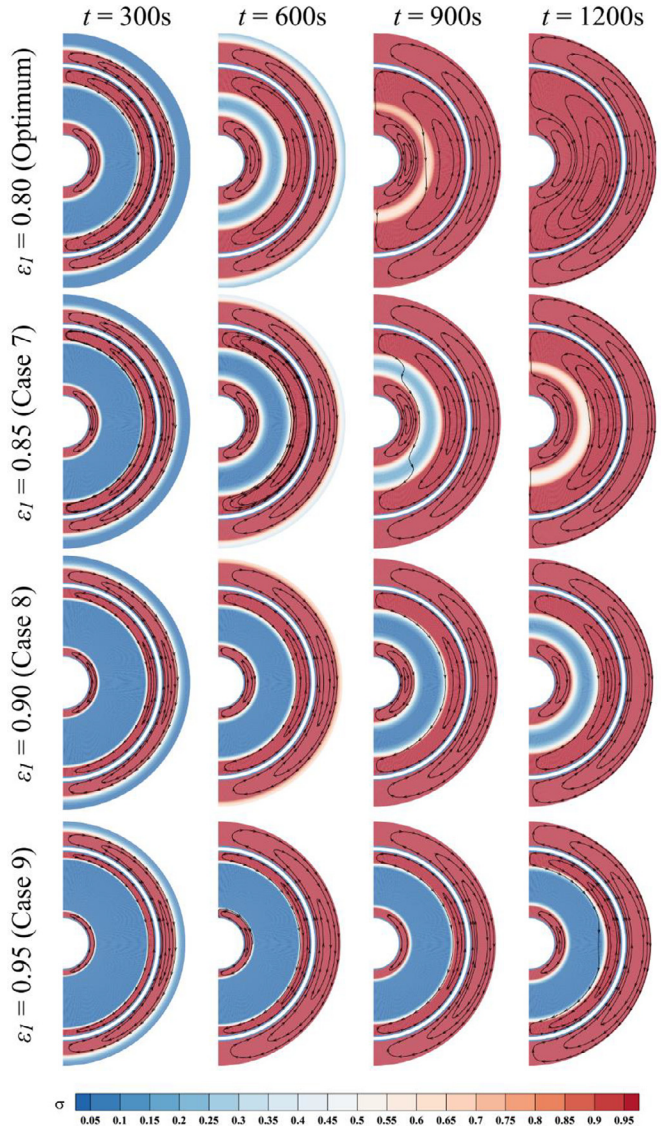

Fig. 9. Effect of porosity of the inner region (ε_1) on the contours of σ (melting fraction) and streamlines (other parameters are same as the optimum case: ω_1 = 0.03, ω_2 = 0.03, ε_2 = 0.8, and r_{o2} = 70 mm).

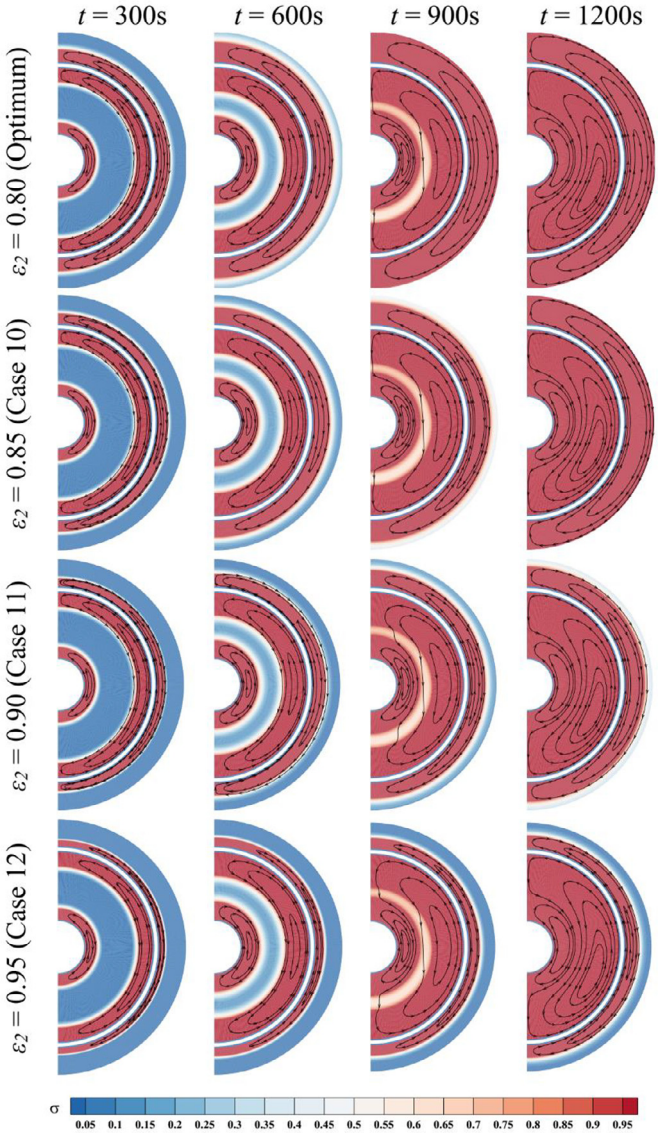

Fig. 10. Effect of porosity of the outer region (ε_2) on the contours of σ (melting fraction) and streamlines (other parameters are same as the optimum case: ω_1 = 0.03, ω_2 = 0.03, ε_1 = 0.8, and r_{o2} = 70 mm).

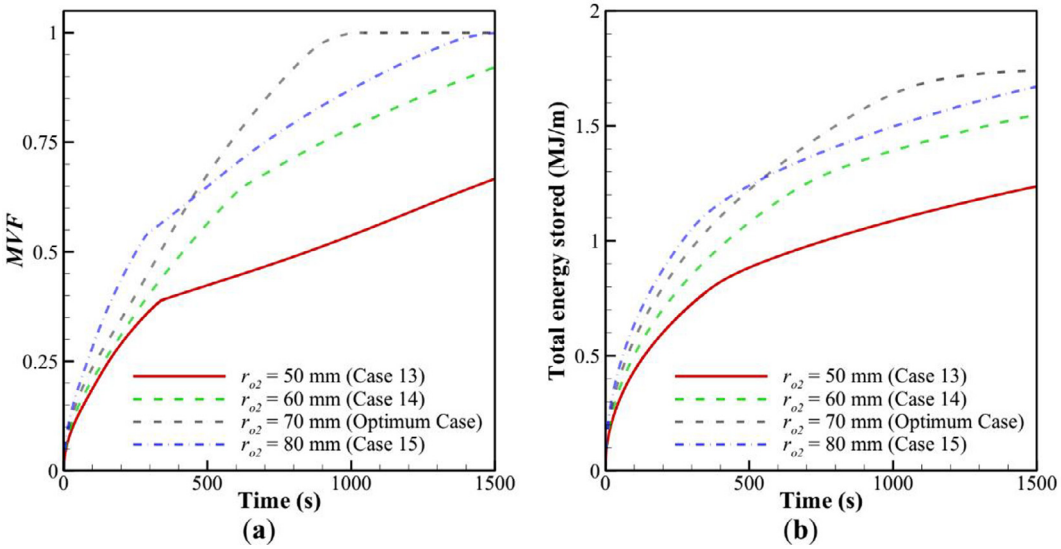

Fig. 11. Effect of r_{o2} on the (**a**) Melted fraction; (**b**) total energy stored (other parameters are same as the optimum case: $\omega_1 = 0.03$, $\omega_1 = 0.03$, $\varepsilon_1 = 0.8$, $\varepsilon_2 = 0.8$).

the variation of porosity induces almost linear impacts on the *MVF*. However, as time passes and *MVF* increases, the natural convection effects get strong and non-linear effects can be seen. There is a significant difference between *MVF*s in the 1200s.

Interestingly, the optimum case maintains superior *MVF* over other cases. However, cases of ε_1 or $\varepsilon_2 = 0.85$ could have the comparable charging time as the optimum case with $\varepsilon_1 = \varepsilon_2 = 0.80$. Thus, a TES with ε_1 or $\varepsilon_2 = 0.85$ could be advantageous since the amount of utilized metal foam material is smaller for a design with higher porosity. Indeed, the case of $\varepsilon_1 = 0.85$ could benefit from both natural convection effects and improved thermal conductivity effects for composite foam and NePCM. In all cases, the optimum design shows better thermal energy storage. A comparison between two special design cases of ε_1 or $\varepsilon_2 = 0.85$ and the optimum case shows that the stored energy for the optimum case is slightly higher. The difference could be due to the sensible heat. A case with lower porosity has a better composite thermal conductivity, and its melted domain gets warm shortly.

Figs. 9 and 10 are plotted to analyze the impact of porosity on melting behaviour in detail. The images were reported for σ (liquid fraction), and the streamlines were plotted in the liquid region to show the natural convection flows. Fig. 9 shows the influence of the increase of ε_1 on the liquid fraction (σ). Since ε_1 is the foam's porosity in the region between the central HTF and narrow heating channel, the variation of σ is more pronounced here. This figure shows that the narrow heating channel is responsible for most of the melting rate. This is because of the larger surface area of the channel, which is in contact with the PCM domain. The melting commences around the central HTF tube and narrow heating channel and advances toward the centre of the NePCM#1. Attention to NePCM#2 shows that this region is almost independent of the first region. It quickly melts down and, at 900s, is in a complete liquid state. Thus, this figure shows that the increase of porosity reduced the molten region in NePCM#1, which agrees with Fig. 8.

Both cases of $\varepsilon_1 = 0.85$ and $\varepsilon_1 = 0.8$ (optimum case) show well developed natural convection flows in the molten NePCM. The closer the streamlines, the stronger the natural convection. Thus, as seen in the time snap of 900s, the natural convection for $\varepsilon_1 = 0.85$ is stronger than $\varepsilon_1 = 0.8$. Thus, the case with a better composite thermal conductivity ($\varepsilon_1 = 0.8$) and a case with a better convection circulation ($\varepsilon_1 = 0.85$) led to the same full melting time.

Fig. 10 illustrates that both cases of $\varepsilon_2 = 0.85$ and $\varepsilon_2 = 0.80$ have almost the same liquid fraction distribution at 900s in the second domain (NePCM#2). The liquid fraction in the first domain (NePCM#1) is independent of ε_2. Thus, the discussion here is mainly related to the second domain under the influence of ε_2. In the case $\varepsilon_2 = 0.85$, there is a narrow un-melted region next to the shell while the optimum case is fully melted. However, case $\varepsilon_2 = 0.85$ benefits from a stronger natural convection flow, and as seen in the nest time snap (t=1200), the second domain is fully melted for both $\varepsilon_2 = 0.80$ and $\varepsilon_2 = 0.85$. The cases of $\varepsilon_2 = 0.90$ and $\varepsilon_2 = 0.95$ follow the same pattern but with a notable delay.

Fig. 11 displays the *MVF* and stored energy for the narrow heating channel radius, r_{o2}. The variation of r_{o2} changed the location of the heating source to the PCM domains. It also changes the size of each domain. The Taguchi analysis showed that r_{o2} is the most influential parameter on the *MVF* of the TES unit. Fig. 11 shows the significant impact of this parameter of *MVF* and ES. The impact of r_{o2} on the early stages of charging, $t < 400$, is smooth. At the beginning of charging, the heat transfer is mainly due to conduction, and the effective thermal conductivity of the composite (foam and NePCM) is not much high. Thus, the heated regions of the TES domain are mainly under the influence of thermal diffusion, and the heat flow has not seen the enclosure boundaries. At this stage, a larger r_{o2} results in a larger heat transfer surface and better heat transfer performance. However, as the thermal charging continues and melting advances in the TES unit, the important effect of r_{o2}, which is the balance of heat between the two domains pronounces. The impact of r_{o2} on the melting heat transfer can be studied through σ contours and streamlines, as depicted in Fig. 12.

A design with a very larger r_{o2} (80 mm) quickly melts down the second domain, NePCM#2, and there is a large NePCM#1 to be melted. Thus, the thermal performance of a case with two large r_{o2} drops quickly. However, a very large r_{o2} (80mm) tends to recover an advantage since the molten region in the NePCM#1 could be quite large and boosts the natural convection effects. The worst case is a case with the smallest r_{o2}. This case provides a small heat transfer surface at the early stages of charging and later results in a small NePCM#1. Thus, at the final stages of charging, domain#1 is fully melted while still half of domian#2 is in a solid state. The optimum case, as proposed by the Taguchi method, is a narrow heating channel with a fairly large radius of $r_{o2} = 70$ mm. Since

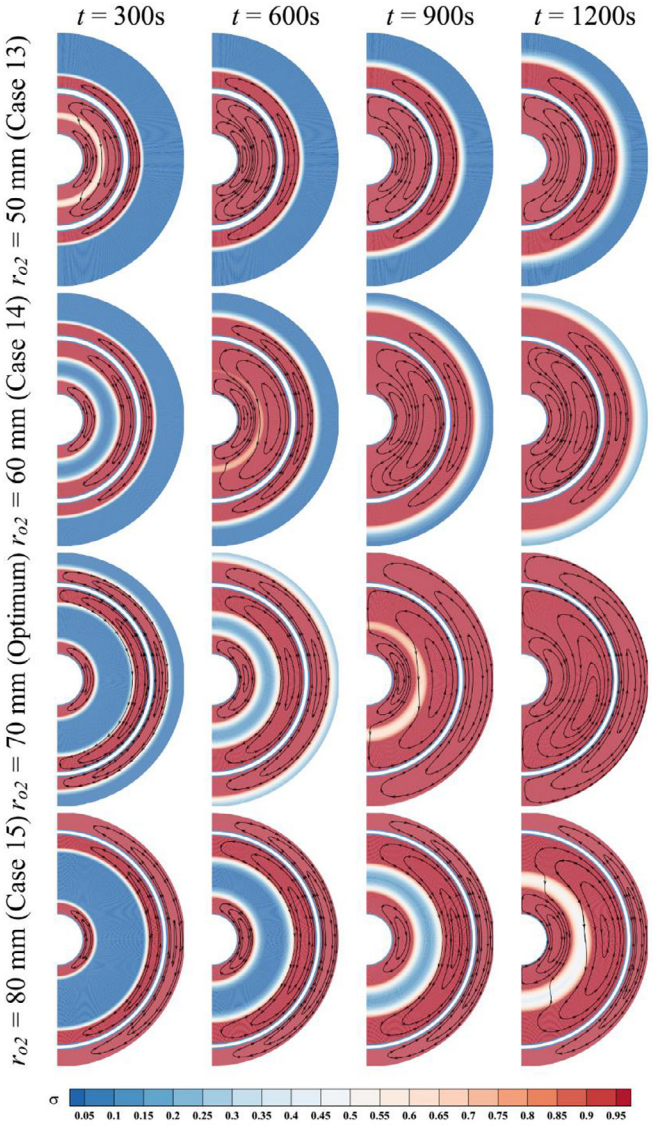

Fig. 12. Effect of r_{o2} on the contours of σ (melting fraction) and streamlines (other parameters are same as the optimum case: $\omega_1 = 0.03$, $\omega_2 = 0.03$, $\varepsilon_2 = 0.8$, $\varepsilon_2 = 0.8$).

the dominant term of energy storage is due to the latent heat, the stored energy in Fig. 10 shows the same trend as that of *MVF*.

6. Conclusions

A combination of metal foam and copper oxide nanoparticles was used to enhance the charging time of a TES unit. The geometrical design of TES, along with its porosities and volume fractions of nanoparticles, were optimized using the Taguchi method. The TES unit could reach a fully melted status just in two hours for the optimum design. The melting rate and the stored energy were investigated using graphs, while the melting behavior and natural convection were studied using liquid fraction contours and streamlines. The following primary results were found:

- The most important parameter affecting the melting rate was the radius of the narrow heating channel, r_{o2}. After that, the porosities of NePCM#2 and NePCM#1 were the most influential parameters. The concentration of nanoparticles could add minor impacts on the melting rate and phase change behaviour.
- The variation of design parameters could change the melting rate by 59%. Thus, the optimization of TES is an important task that should be considered in the design of TES units.
- The increase of the volume fraction of the copper oxide nanoparticles does not always improve the melting rate. The optimum volume fraction of nanoparticles was 3%, while the maximum investigated value was 4.5%. As seen, the maximum volume fraction did not lead to the maximum melting rate. Moreover, the impact of the presence of nanoparticles on the melting rate was not significant. Thus, the application of nanoparticles in the TES units enhanced with metal foams cannot be justified.
- The geometrical design of TES was carried out for the radius of the narrow heating channel, r_{o2}. The optimum radius was 70 mm while the range of the variation of this parameter was 50-80mm. The *MVF* for design with $r_{o2} = 50$mm was 0.59 after two hours of thermal charging, while the same design but $r_{o2} = 70$ resulted in full melting (*MVF* = 1.0). Thus, the optimal geometrical design of a TES is the most important task and should be carefully considered in future studies. After that, other heat transfer approaches could be applied to improve the heat transfer further.

A fast-charging TES unit can be used in many practical applications such as transient waste heat recovery, thermal management of transient industrial systems, and process engineering. In the present study, the utilized PCM in both domains of the TES unit was the same. However, the present design could benefit from two different PCMs with different fusion temperatures, which could be the subject of future investigations.

Funding

This research received no external funding.

Data availability statement

The data will be available on request.

Declaration of Competing Interest

The authors declare no conflict of interest.

CRediT authorship contribution statement

Seyed Mohsen Hashem Zadeh: Conceptualization, Methodology, Validation, Formal analysis, Data curation. **Maryam Ghodrat:** Conceptualization, Methodology, Supervision, Writing – original draft, Writing – review & editing. **Kaamran Raahemifar:** Conceptualization, Investigation, Writing – review & editing. **Obai Younis:** Conceptualization, Methodology, Writing – original draft, Writing – review & editing. **Mohammad Ghalambaz:** Conceptualization, Methodology, Supervision, Writing – original draft, Writing – review & editing.

Acknowledgments

This work was supported by computational resources provided by the Australian Government through University of New South Wales under the National Computational Merit Allocation Scheme.

References

[1] K. Reddy, V. Mudgal, T. Mallick, Review of latent heat thermal energy storage for improved material stability and effective load management, J. Energy Storage 15 (2018) 205–227.

[2] S.S. Magendran, F.S.A. Khan, N. Mubarak, M. Vaka, R. Walvekar, M. Khalid, E. Abdullah, S. Nizamuddin, R.R. Karri, Synthesis of organic phase change materials (PCM) for energy storage applications: a review, Nano-Struct. Nano-Objects 20 (2019) 100399.
[3] A. Agarwal, R. Sarviya, Characterization of commercial grade paraffin wax as latent heat storage material for solar dryers, Mater. Today: Proc. 4 (2) (2017) 779–789.
[4] A. Shahsavar, A. Goodarzi, H.I. Mohammed, A. Shirneshan, P. Talebizadehsardari, Thermal performance evaluation of non-uniform fin array in a finned double-pipe latent heat storage system, Energy 193 (2020) 116800.
[5] A. Shinde, S. Arpit, P. KM, P.V.C. Rao, S.K. Saha, Heat transfer characterization and optimization of latent heat thermal storage system using fins for medium temperature solar applications, J. Sol. Energy Eng. 139 (3) (2017).
[6] S. Tiari, M. Mahdavi, S. Qiu, Experimental study of a latent heat thermal energy storage system assisted by a heat pipe network, Energy Convers. Manage. 153 (2017) 362–373.
[7] J. Gasia, D. Groulx, N.S. Tay, L.F. Cabeza, Numerical study of dynamic melting enhancement in a latent heat thermal energy storage system, Jo. Energy Storage 31 (2020) 101664.
[8] N. Tay, F. Bruno, M. Belusko, Experimental investigation of dynamic melting in a tube-in-tank PCM system, Appl. Energy 104 (2013) 137–148.
[9] T. Xiong, Y. Wang, X. Yang, Numerical investigation of dynamic melting process in a thermal energy storage system using U-tube heat exchanger, Adv. Mech. Eng. 9 (5) (2017) 1687814017707415.
[10] X. Yang, T. Xiong, J.L. Dong, W.X. Li, Y. Wang, Investigation of the dynamic melting process in a thermal energy storage unit using a helical coil heat exchanger, Energies 10 (8) (2017) 1129.
[11] J. Gasia, A. de Gracia, G. Peiró, S. Arena, G. Cau, L.F. Cabeza, Use of partial load operating conditions for latent thermal energy storage management, Appl. Energy 216 (2018) 234–242.
[12] J. Gasia, A. de Gracia, G. Zsembinszki, L.F. Cabeza, Influence of the storage period between charge and discharge in a latent heat thermal energy storage system working under partial load operating conditions, Appl. Energy 235 (2019) 1389–1399.
[13] S. Arena, E. Casti, J. Gasia, L.F. Cabeza, G. Cau, Numerical analysis of a latent heat thermal energy storage system under partial load operating conditions, Renewable Energy 128 (2018) 350–361.
[14] Z.-Q. Zhu, Y.-K. Huang, N. Hu, Y. Zeng, L.-W. Fan, Transient performance of a PCM-based heat sink with a partially filled metal foam: Effects of the filling height ratio, Appl. Therm. Eng. 128 (2018) 966–972.
[15] M.M. El Idi, M. Karkri, M. Kraiem, Preparation and effective thermal conductivity of a Paraffin/Metal Foam composite, J. Energy Storage (2020) 102077.
[16] J. Duan, F. Li, Transient heat transfer analysis of phase change material melting in metal foam by experimental study and artificial neural network, J. Energy Storage, 33 102160.
[17] M. Irwan, C.N. Azwadi, Y. Asako, J. Ghaderian, Review on numerical simulations for nano-enhanced phase change material (NEPCM) phase change process, J. Therm. Anal. Calorim. (2019) 1–16.
[18] M. Irwan, C.N. Azwadi, Y. Asako, Review on numerical simulations for solidification & melting of nano-enhanced phase change materials (NEPCM), IOP Conference Series: Earth and Environmental Science, IOP Publishing, 2019.
[19] V. Selvaraj, B. Morri, L.M. Nair, H. Krishnan, Experimental investigation on the thermophysical properties of beryllium oxide-based nanofluid and nano-enhanced phase change material, J. Therm. Anal. Calorim. 137 (5) (2019) 1527–1536.
[20] H. Faraji, M. El Alami, A. Arshad, Investigating the effect of single and hybrid nanoparticles on melting of phase change material in a rectangular enclosure with finite heat source, Int. J. Energy Res. (2020).
[21] M.B. Akash, R. Harish, M.S. Kumar, Thermal performance of nanoparticle enhanced phase change material in a concentric cylindrical enclosure, IOP Conference Series: Earth and Environmental Science, IOP Publishing, 2020.
[22] N.H. Boukani, A. Dadvand, A.J. Chamkha, Melting of a nano-enhanced phase change material (NePCM) in partially-filled horizontal elliptical capsules with different aspect ratios, Int. J. Mech. Sci. 149 (2018) 164–177.
[23] M. Sheikholeslami, Solidification of NEPCM under the effect of magnetic field in a porous thermal energy storage enclosure using CuO nanoparticles, J. Mol. Liq. 263 (2018) 303–315.
[24] J.M. Mahdi, E.C. Nsofor, Melting enhancement in triplex-tube latent heat energy storage system using nanoparticles-metal foam combination, Appl. Energy 191 (2017) 22–34.
[25] M. Alomair, Y. Alomair, S. Tasnim, S. Mahmud, H. Abdullah, Analyses of bio-based nano-PCM filled concentric cylindrical energy storage system in vertical orientation, J. Energy Storage 20 (2018) 380–394.
[26] M. Al-Jethelah, S. Ebadi, K. Venkateshwar, S.H. Tasnim, S. Mahmud, A. Dutta, Charging nanoparticle enhanced bio-based PCM in open cell metallic foams: an experimental investigation, Appl. Therm. Eng. 148 (2019) 1029–1042.
[27] V. Joshi, M.K. Rathod, Experimental and numerical assessments of thermal transport in fins and metal foam infused latent heat thermal energy storage systems: A comparative evaluation, Appl. Therm. Eng. 178 (2020) 115518.
[28] A. Hussanan, M.Z. Salleh, I. Khan, S. Shafie, Convection heat transfer in micropolar nanofluids with oxide nanoparticles in water, kerosene and engine oil, J. Mol. Liq. 229 (2017) 482–488.
[29] D.A. Nield, A. Bejan, Convection in Porous Media, Springer Science & Business Media, 2006.
[30] J. Buongiorno, Convective transport in nanofluids, J. Heat Transfer 128 (3) (2006) 240–250.
[31] M. Sheikholeslami, M. Shamlooei, R. Moradi, Fe3O4-Ethylene glycol nanofluid forced convection inside a porous enclosure in existence of Coulomb force, J. Mol. Liq. 249 (2018) 429–437.
[32] M. Hameter, H. Walter, Influence of the Mushy zone constant on the numerical simulation of the melting and solidification process of phase change materials, in: Z. Kravanja, M. Bogataj (Eds.), Computer Aided Chemical Engineering, Elsevier, 2016, pp. 439–444.
[33] M. Fadl, P.C. Eames, Numerical investigation of the influence of mushy zone parameter Amush on heat transfer characteristics in vertically and horizontally oriented thermal energy storage systems, Appl. Therm. Eng. 151 (2019) 90–99.
[34] A. Shahsavar, A.A.A.A. Al-Rashed, S. Entezari, P.T. Sardari, Melting and solidification characteristics of a double-pipe latent heat storage system with sinusoidal wavy channels embedded in a porous medium, Energy 171 (2019) 751–769.
[35] P.T. Sardari, H.I. Mohammed, D. Giddings, G.S. walker, M. Gillott, D. Grant, Numerical study of a multiple-segment metal foam-PCM latent heat storage unit: Effect of porosity, pore density and location of heat source, Energy 189 (2019) 116108.
[36] P. Ranut, On the effective thermal conductivity of aluminum metal foams: Review and improvement of the available empirical and analytical models, Appl. Therm. Eng. 101 (2016) 496–524.
[37] O. Mesalhy, K. Lafdi, A. Elgafy, K. Bowman, Numerical study for enhancing the thermal conductivity of phase change material (PCM) storage using high thermal conductivity porous matrix, Energy Convers. Manage. 46 (6) (2005) 847–867.
[38] H. Zheng, C. Wang, Q. Liu, Z. Tian, X. Fan, Thermal performance of copper foam/paraffin composite phase change material, Energy Convers. Manage. 157 (2018) 372–381.
[39] Q. Ren, Enhancement of nanoparticle-phase change material melting performance using a sinusoidal heat pipe, Energy Convers. Manage. 180 (2019) 784–795.
[40] H.C. Brinkman, The viscosity of concentrated suspensions and solutions, J. Chem. Phys. 20 (4) (1952) 571-571.
[41] S. Kakaç, A. Pramuanjaroenkij, Review of convective heat transfer enhancement with nanofluids, Int. J. Heat Mass Transfer 52 (13) (2009) 3187–3196.
[42] A.C. Kheirabadi, D. Groulx, The effect of the mushy-zone constant on simulated phase change heat transfer, in: Proceedings of CHT-15. 6 th International Symposium on Advances in Computational Heat Transfer, Begel House Inc., 2015.
[43] S. Arena, E. Casti, J. Gasia, L.F. Cabeza, G. Cau, Numerical simulation of a finned-tube LHTES system: influence of the mushy zone constant on the phase change behaviour, Energy Procedia 126 (2017) 517–524.
[44] M. Kumar, D.J. Krishna, Influence of mushy zone constant on thermohydraulics of a PCM, Energy Procedia 109 (2017) 314–321.
[45] A. Freddi, M. Salmon, Introduction to the Taguchi method, in: Design Principles and Methodologies, Springer, 2019, pp. 159–180.
[46] K. Krishnaiah, P. Shahabudeen, Applied Design of Experiments and Taguchi Methods, PHI Learning Pvt. Ltd., 2012.